

Supporting Information:

Bimetallic cyclic redox couple in di-manganese copper oxide supported by nickel borate for boosted alkaline electrocatalytic oxygen evolution reaction

*Sourav Bhowmick, Suhaib Alam, Adit Kumar Shah, Mohammad Qureshi**

Department of Chemistry, Indian Institute of Technology Guwahati, Assam- 781039, India.

*** Corresponding Author**

E-mail: mq@iitg.ac.in (M. Q.)

Materials Characterization

X-ray diffraction measurement was accomplished using a Rigaku Smartlab X-ray diffractometer with copper K_{α} ($\lambda=1.54$ Å) as source with 9 kW power. XRD patterns were recorded from 2θ ($10 - 70^\circ$) keeping the scan rate fix at 4° s^{-1} . To determine the morphological features of the samples, field emission scanning electron microscopy (FESEM) analysis was carried out using a Zeiss (model-Gemini and Sigma) instrument operated at 5kV. A JEOL (JEM-2100F) transmission electron microscope with an operating voltage of 200 kV was used for field emission transmission electron microscopy (FETEM) analysis of the samples. A CH Instruments model CHI760E, Inc., Austin, TX, was used to record the cyclic voltammetry (CV) and electrochemical impedance spectroscopy (EIS). Gas chromatography (GC) (Model-7820A, Agilent Technologies) was used to measure the evolved gasses and to calculate faradaic efficiency.

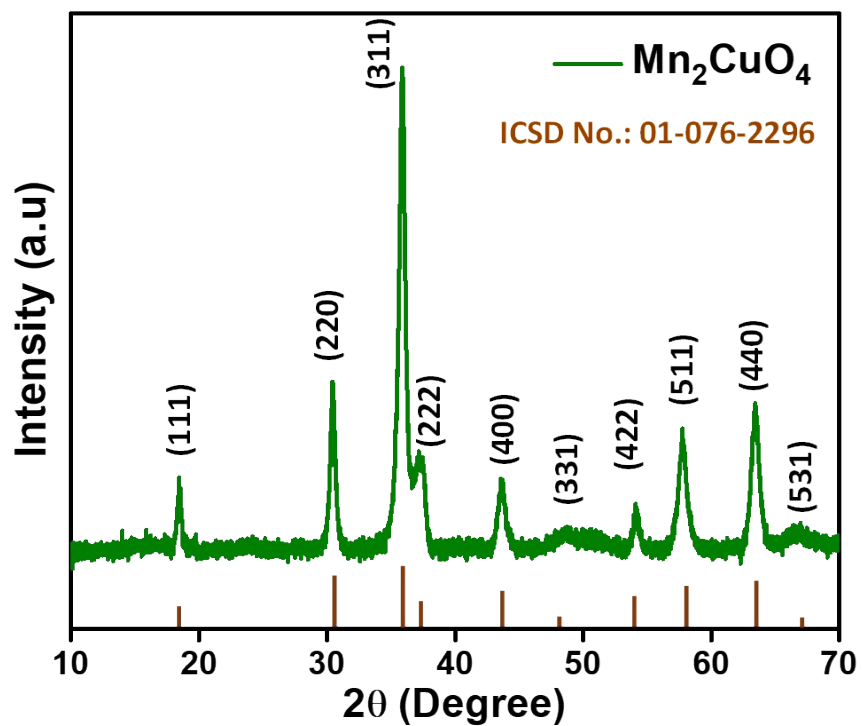


Figure S1. PXRD of the synthesized Mn_2CuO_4 powder with all the peaks indexable to the cubic phase of di-manganese copper oxide (ICSD No. 01-076-2296)

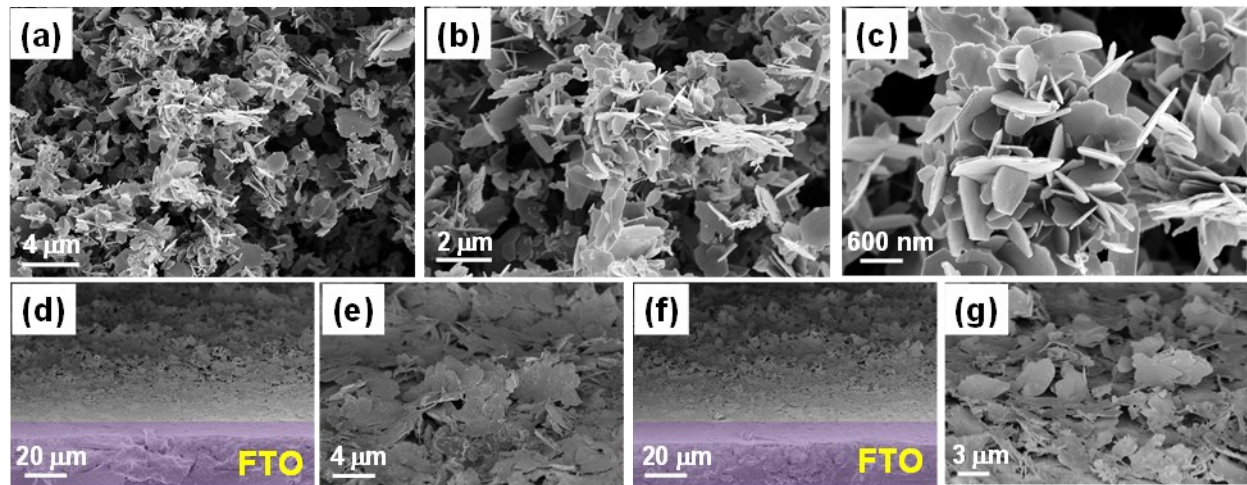


Figure S2. (a-c) FESEM images of the synthesized Mn_2CuO_4 powder, cross-sectional view of the fabricated electrode of (d, e) bare Mn_2CuO_4 , and (f, g) $\text{Mn}_2\text{CuO}_4/\text{Ni-B}_i$

From the figure, it is clear that the morphology of the catalyst is intact upon the fabrication of bare and modified electrocatalyst over FTO.

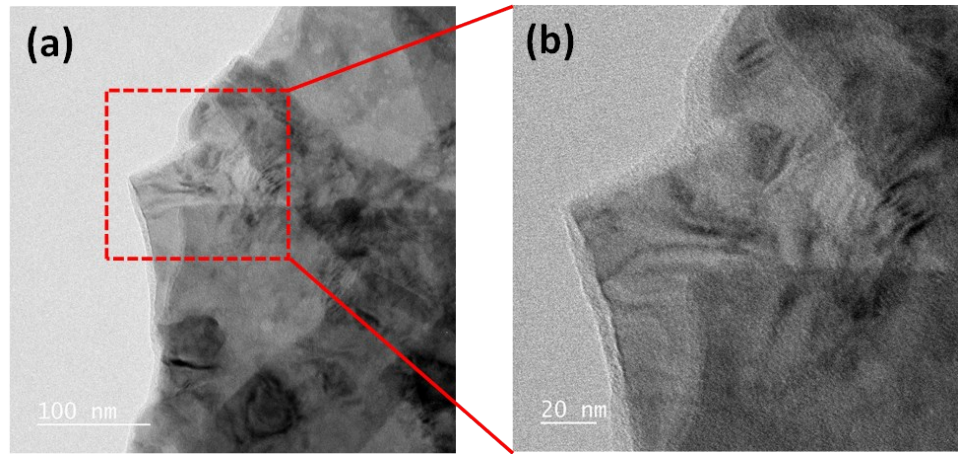


Figure S3. FETEM images of the composite $\text{Mn}_2\text{CuO}_4/\text{Ni-B}_i$ showing the uniform deposition of nickel borate over the surface

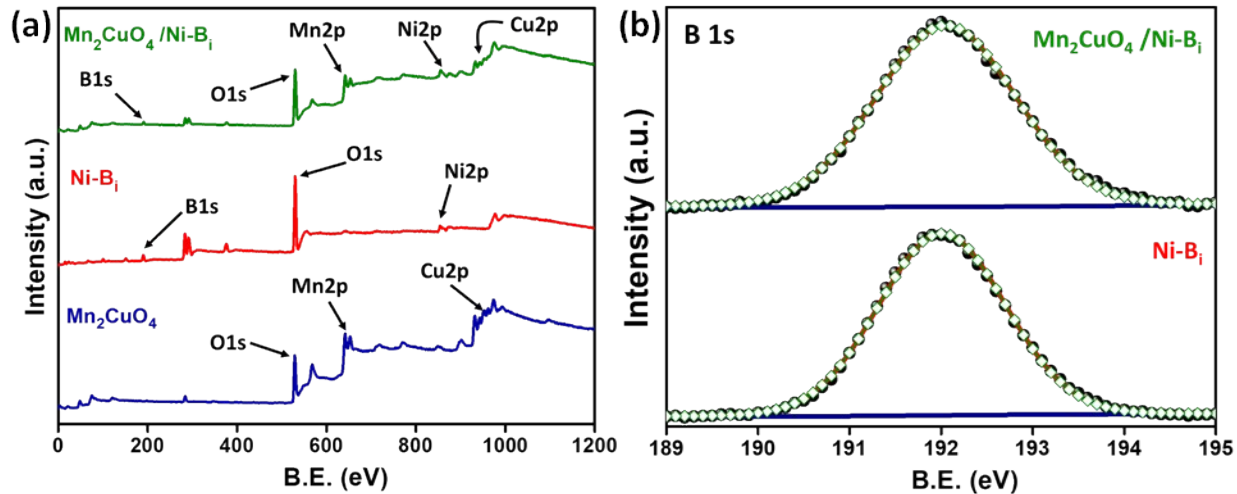


Figure S4. (a) XPS survey spectra of Mn_2CuO_4 , Ni-B_i , and $\text{Mn}_2\text{CuO}_4/\text{Ni-B}_i$ confirming the presence of all the respective elements, (b) 1s core-level spectra of boron for Ni-B_i and $\text{Mn}_2\text{CuO}_4/\text{Ni-B}_i$

The XPS survey spectra (Fig. S4 (a)) of Mn_2CuO_4 , Ni-B_i , and $\text{Mn}_2\text{CuO}_4/\text{Ni-B}_i$ shows the presence of the respective elements in the compounds. The 1s core-level spectra of boron are shown in Fig. S4 (b). The peak at a binding energy of 192.01 eV is for bare nickel borate, and for the composite, $\text{Mn}_2\text{CuO}_4/\text{Ni-B}_i$, the peak is shifted to 192.05 eV.^{1,2} The shift in the peak position towards higher binding energy is due to the interaction of nickel borate with di-manganese copper oxide.

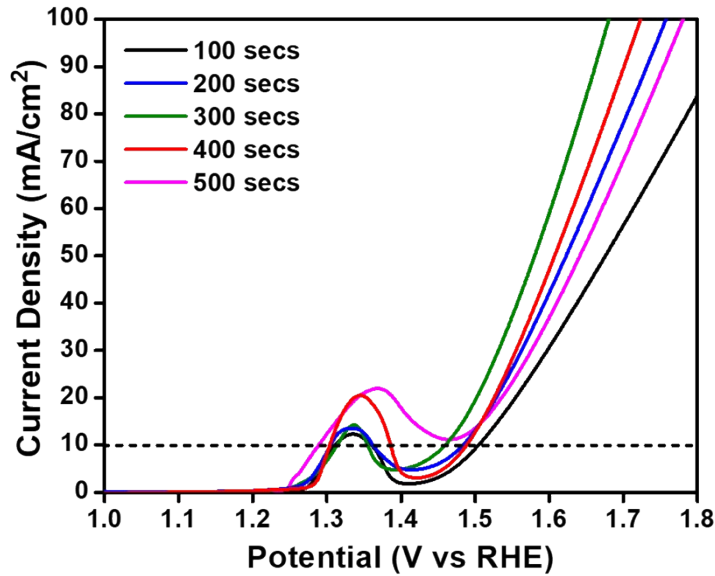


Figure S5. Linear sweep voltammograms (LSV) of Mn₂CuO₄/Ni-B_i for the optimization of nickel borate deposition over the Mn₂CuO₄ surface

As can be seen from the figure, the performance of the electrocatalyst is dependent on the time of deposition of Ni-B_i over the Mn₂CuO₄ surface. The optimum deposition time is found out to be 5 min (300 sec). The excessive deposition of Ni-B_i overcrowds the surface leading to the decrease in the active surface area for the catalytic reaction, henceforth the performance decreases with the increase in the deposition time (400 sec and 500 sec).

Table S1. The charge transfer resistance (R_{ct}) values obtained by fitting the Nyquist plots

Potential (vs RHE)	Condition	Compound	R_{ct} (Ω)
1.5 V	Before cross-over	Mn ₂ CuO ₄ /Ni-B _i	144.9
		RuO ₂	97.24
1.55 V	At cross-over	Mn ₂ CuO ₄ /Ni-B _i	48.3
		RuO ₂	49.54
1.6 V	After cross-over	Mn ₂ CuO ₄ /Ni-B _i	13.15
		RuO ₂	23.47

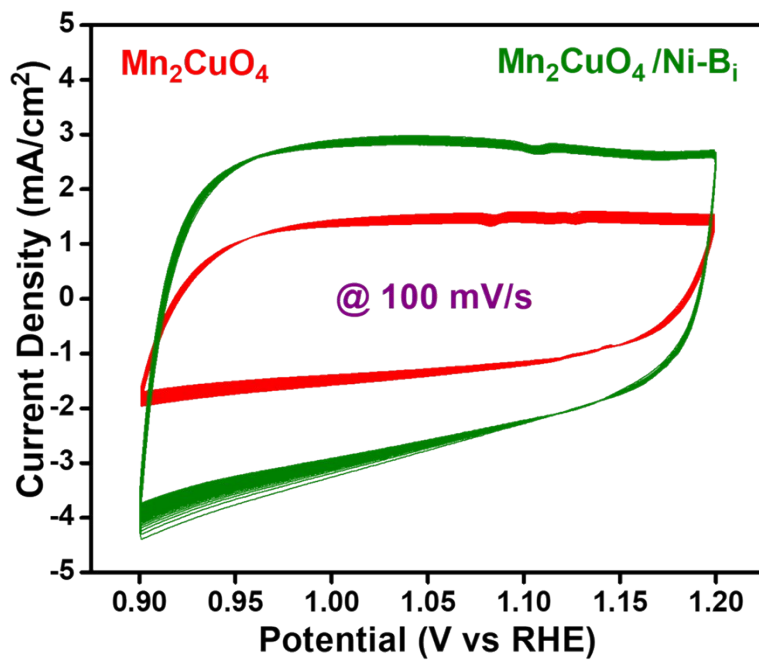


Figure S6. CV plots of 1000 cycles for testing the durability of Mn_2CuO_4 and $\text{Mn}_2\text{CuO}_4/\text{Ni-B}_i$ measured at a scan rate of 100 mV/s

From Fig. S6, it can be inferred that the durability of both bare Mn_2CuO_4 and modified $\text{Mn}_2\text{CuO}_4/\text{Ni-B}_i$ is high even after a continuous run of 1000 cycles. The high stability of both the catalyst is due to the self-healing redox cycle of bimetallic Cu and Mn in di-manganese copper oxide and Ni in nickel borate.

Table S2. Comparison between the recently developed electrocatalysts

Catalyst	Electrolyte	Overpotential (mV) at specific current density	Tafel slope (mV/dec)	Reference
Mn₂CuO₄	1M NaOH	420 @ 10 mA/cm²	104	This work
Mn₂CuO₄ /Ni-B_i	1M NaOH	230 @ 10 mA/cm²	56	This work
Ni-B _i /CC	0.1M K-B _i	470 @ 10 mA/cm ²	107	S1
Ni-B _i -P _i /CC	0.1M K-B _i	440 @ 10 mA/cm ²	139	S2
IrO ₂	0.1M KOH	450 @ 10 mA/cm ²	83	S3
RuO ₂	0.5M KOH	425 @ 10 mA/cm ²	55	S4
Mn ₂ O ₃	1M KOH	270 @ 10 mA/cm ²	85	S5
Mn ₃ O ₄ -CoMn ₂ O ₄	0.1M KOH	310 @ 10 mA/cm ²	81	S6
Co(PO ₃) ₂	0.1M NaPi	440 @ 8 mA/cm ²	74	S7
Co ₃ O ₄	0.1M KOH	400 @ 10 mA/cm ²	49	S8
Mn _x Co _{3-x} O ₄	0.1M KOH	350 @ 10 mA/cm ²	85	S9
CoFe ₂ O ₄	0.1M KOH	370 @ 10 mA/cm ²	82	S10
MnCo ₂ O ₄	1M KOH	327 @ 10 mA/cm ²	79	S11
Mn ₂ CoO ₄	1M KOH	399 @ 10 mA/cm ²	79	S11
CuCo ₂ O ₄	0.5M KOH	327 @ 10 mA/cm ²	74	S12
NiCo ₂ O ₄	0.1M KOH	320 @ 10 mA/cm ²	87	S12
V-doped Co ₃ O ₄	1M KOH	294 @ 10 mA/cm ²	53	S13
V-doped NiFe ₂ O ₄	1M KOH	270 @ 10 mA/cm ²	42	S13
Co-B _i	0.5M K-B _i	285 @ 10 mA/cm ²	166	S14

References

- S1. X. Ji, L. Cui, D. Liu, S. Hao, J. Liu, F. Qu, Y. Ma, G. Du, A. M. Asiri and X. Sun, *Chem. Commun.*, 2017, **53**, 3070–3073.
- S2. M. Ma, D. Liu, S. Hao, R. M. Kong, G. Du, A. M. Asiri, Y. D. Yao and X. P. Sun, *Inorg. Chem. Front.*, 2017, **4**, 840–844.
- S3. H. Sun, X. Xu, Z. Hu, L. H. Tjeng, J. Zhao, Q. Zhang, H. J. Lin, C. Te Chen, T. S. Chan, W. Zhou and Z. Shao, *J. Mater. Chem. A*, 2019, **7**, 9924–9932.
- S4. W. Ma, R. Ma, C. Wang, J. Liang, X. Liu, K. Zhou and T. Sasaki, *ACS Nano*, 2015, **9**, 1977–1984.
- S5. P.-P. Liu, Y.-Q. Zheng, H.-L. Zhu, and T.-T. Li, *ACS Appl. Nano Mater.*, 2019, **2**, 744–749.
- S6. Z. Luo, E. Irtem, M. Ibáñez, R. Nafria, S. Martí-Sánchez, A. Genc, M. de la Mata, Y. Liu, D. Cadavid, J. Llorca, J. Arbiol, T. Andreu, J. R. Morante and A. Cabot, *ACS Appl. Mater. Interfaces*, 2016, **8**, 17435–17444.
- S7. J. G. McAlpin, Y. Surendranath, M. Dinca, T. A. Stich, S. A. Stoian, W. H. Casey, D. G. Nocera and R. D. Britt, *J. Am. Chem. Soc.*, 2010, **132**, 6882–6883.
- S8. J. A. Koza, Z. He, A. S. Miller and J. A. Switzer, *Chem. Mater.*, 2012, **24**, 3567–3573.
- S9. T. Y. Ma, S. Dai, M. Jaroniec and S. Z. Qiao, *Chem.–Eur. J.*, 2014, **39**, 12669.
- S10. M. Li, Y. Xiong, X. Liu, X. Bo, Y. Zhang, C. Han and L. Guo, *Nanoscale*, 2015, **7**, 8920–8930.
- S11. K. Lankauf, K. Cysewska, J. Karczewski, A. M.-Gryń, K. Górnick, G. Cempura, M. Chen, P. Jasiński, S. Molin, *International Journal of Hydrogen Energy*, 2020, **45**, 14867–14879.

- S12. G. Janani, Y. Chae, S. Surendran, Y. Sim, W. Park, J. K. Kim, and U. Sim, *Appl. Sci.*, 2020, **10**, 3165.
- S13. R. Wei, X. Bu, W. Gao, R. Angelo, B. Villaos, G. Macam, Z.-Q. Huang, C. Lan, F.-C. Chuang, Y. Qu, and J. C. Ho, *ACS Appl. Mater. Interfaces*, 2019, **11**, 33012–33021.
- S14. R. Ge, H. Du, K. Tao, Q. Zhang, and L. Chen, *ACS Appl. Mater. Interfaces*, 2017, **9**, 15383–15387.